Bimetal ZIF-9-Derived N-doped Porous Carbons as High-Efficient Oxygen Electrocatalysts for Rechargeable Zn-Air Batteries

Afshin Pendashteh,[a,1] Sérgio M. F. Vilela,[b] Igor Krivtsov,[c] David Ávila-Brande,[d] Jesus Palma [a], Patricia Horcajada,[b,]* and Rebeca Marcilla [a,]*

[a] Electrochemical Processes Unit, [b] Advanced Porous Materials Unit (APMU), IMDEA Energy Institute, Parque Tecnológico de Móstoles, Avda. Ramón de la Sagra 3, E-28935 Móstoles, Madrid, Spain.

E-mail: patricia.horcajada@imdea.org; rebeca.marcilla@imdea.org

[c]

[d] Departamento de Química Inorgánic, Facultad de Ciencias Químicas, Universidad Complutense, E-28040 Madrid, Spain

---

[1] Current Address: CIC Energigune, Alava Technology Park, Albert Einstein 48, 01510 Miñano Álava, Spain.

ABSTRACT (Word Style "BD_Abstract"). All manuscripts must be accompanied by an abstract. The abstract should briefly state the problem or purpose of the research, indicate the theoretical or experimental plan used, summarize the principal findings, and point out major conclusions. Abstract length is one paragraph.

KEYWORDS (Word Style "BG_Keywords"). If you are submitting your paper to a journal that requires keywords, provide significant keywords to aid the reader in literature retrieval.

INTRODUCTION

Despite of being promising candidates for sustainable and green energy storage devices due to their ultrahigh theoretical energy densities, metal-air batteries' vast commercialization is mainly hindered due to high cost of platinum (Pt)-based catalysts for oxygen reduction (ORR) and precious ruthenium- or Iridium-based catalysts for oxygen evolution (OER) reactions.[1] In recent years, extensive efforts have been made to introduce/develop highly-efficient and low-cost oxygen catalysts, resulting in development of different electrocatalysts including non-precious metal compounds like oxides,[2, 3] hydroxides,[4] nitrides,[5] sulfides[6] or even metal-free electrocatalyst such as carbonaceous materials.[7] Accordingly, significant advances for transition metal oxides were achived through tuning morphology, enhancing surface area and/or by hybridizing with carbonaceous supports such as graphene or carbon nanotubes.[8-11] Metal−organic frameworks (MOF), also known as Porous Coordination Polymers (PCPs) are a recent class of tunable hybrid materials, resulting from the self-assembly of inorganic units (atoms, clusters, chains, etc.) with organic polycomplexant linkers (carboxylates, azolates, phosphonates, among other N- and/or O-donor molecules).[12-14] Compared with other classical porous materials (*e.g.*, active carbons, zeolites and silica), MOFs present very high regular porosity with different shapes and sizes (up to 4.4 cm^3 g^{-1}; S_{BET} = 7000 m^2 g^{-1}; pore diameter = 3-98 Å),[15, 16] and an easy tunable hybrid composition and structure with chemical, mechanical and thermal robustness, allowing the modulation of their physicochemical properties. With that, MOFs are promising candidates for many strategic societal and industrial applications such as fluid storage and separation, catalysis, sensing, biomedicine and energy, among others. Although not extensively explored in the energy field, excepting for the purification and storage of hydrogen,[17, 18] MOFs have shown promising applicability as, for instance, in photocatalysis

(production of H_2 and valorization of CO_2),[19, 20] fuel cell components as proton conductors[21] and batteries,[22] among others.

Among different MOFs, zeolitic imidazolate frameworks (ZIFs) have attracted more attention in synthesis of highly efficient M−N−C electrocatalysts for oxygen reactions due to their large specific surface area and periodically ordered TM−N_4 coordination substructures. However, pyrolysis of ZIFs usually results in uneven decomposition and severe agglomeration of metal-cores, low N-doping, and drastic decrease of the specific surface area which results in insufficient electrocatalytic activity of the final compound. Therefore, a rational design of the ZIF precursors by tunning their compositions and microstructures, for example by doping the structure with other metal ions, can provide a rational and effective way to synthesize high-performance electrocatalysts towards oxygen reactions.

Herein, we develop a novel and simple route to synthesize iron- cobalt- and nitrogen-doped porous carbon as high performance and efficient bifunctional electrocatalysts for ORR/OER via directly pyrolyzing Fe/Co bimetal ZIF-9 crystals. The presence of Fe^{2+} resulted in enhanced surface area of the ZIF-9 precursor after pyrolysis and resulted in uniform codoping of Fe, Co, and N in carbon matrix. By optimizing the amount of Fe^{2+} doped species, the **ZIF-9_Fe3_Pyrol** sample exhibited high electrocatalytic activity and durability towards ORR and OER, suggesting the sample as a promising bifunctional catalysts for rechargeable metal-air batteries.

EXPERIMENTAL SECTION

General Instrumentation

X-ray powder diffraction (XRPD) patterns were collected in a D8 Advance Bruker diffractometer with Cu Kα1 radiation ($\lambda = 1.54056$ Å) from 3 to 35° (2θ) using a step size of 0.02° and 2.5 s per step in continuous mode.

Scanning electron microscopy (SEM) images toward the morphology of all compounds were collected on a Hitachi TM-100 microscope operating at 15 kV.

High resolution transmission electron microscopy (HRTEM) and electron energy loss spectroscopy (EELS) experiments were performed with a JEOL JEM 3000F microscope operating at 300 kV (double tilt (±20°) point resolution 0.17 nm), fitted with an energy-dispersive X-ray spectroscopy (XEDS) microanalysis system (OXFORD INCA) and ENFINA spectrometer with an energy resolution of 1.3 eV. ZIF-9_Fe3_Pyrol for electron microscopy observation was previously prepared by depositing on a carbon-coated grid the suspension resulting from grinding it in n-butyl alcohol and ultrasonically dispersing it.

Fourier Transform Infrared (FTIR) spectrum was recorded in a Thermo Nicolet spectrometer (Thermo, USA) from 4000-400 cm^{-1}.

N_2 sorption measurements were carried out at 77 K on a Belsorp Max® porosimeter (BEL Japan Inc.). Prior to the measurements, samples were degassed under secondary vacuum and heated at 150 °C for 4 h (ZIF-9 and Fe^{2+}-doped ZIF-9) and at 100 °C for 2 h (all pyrolyzed samples). Inductively coupled plasma optic emission spectroscopy (ICP-OES) was carried out in a Perkin Elmer Optima 7300 DV equipment, using Ar as plasma, auxiliary and aerosol gas with flow rates of 15, 0.2 and 0.8 L·min^{-1}, respectively, and a sample flow rate of 1.5 mL·min^{-1}. Previously to

analyses, samples were submitted to a digestion in acidic medium at 100 ºC for 12 h in a sealed reactor.

X-ray photoelectron spectroscopy (XPS) spectra were recorded with a SPECS equipped with a monochromator X-ray source of aluminium (E = 1486.7 eV) operating at 13 kV, 250 W and 19.4 mA.

Reagents and Solvents

Benzimidazole (Acros Organics, 98%), cobalt nitrate hexahydrate ($Co(NO_3)_2 \cdot 6H_2O$, Alfa Aesar, 98%), iron chloride tetrahydrate ($FeCl_2 \cdot 4H_2O$, Sigma Aldrich, 99%) and *N,N´-*dimethylformamide (DMF, Chem-Lab, 99.5%). In the case of other reagents, all were provided from *Sigma-Aldrich* unless otherwise specified. All reagents and solvents were used as received for the commercial suppliers without further purification.

Synthesis of ZIF-9

ZIF-9 was prepared according to a similar synthetic procedure previously reported by Yaghi's group with some modifications.[23] A reactive mixture composed of benzimidazole (0.126 g) and ($Co(NO_3)_2 \cdot 6H_2O$ (0.210 g), with a 1:1.5 (metal:ligand) molar ratio, in 18 mL of DMF was prepared in a 20-mL glass vial being then, capped and stirred for 5 min. The vial was transferred into an oven following the temperature program: heating from room temperature to 130 ºC at a rate of 5 ºC·min^{-1}, held at this temperature for 48 h and cooling to 30 ºC at a rate of 0.4 ºC·min^{-1}. The resulting purple crystals where recovered by filtration, washed with copious amounts of DMF and air-dried.

Synthesis of Fe^{2+}-doped ZIF-9 compounds

All the isotypical Fe^{2+}-doped ZIF-9 samples were prepared by using the same aforementioned procedure. The only difference resides in the: i) adjustment of Co^{2+} and Fe^{2+}

contents in order to isolate ZIF-9 with different percentages of Fe^{2+} in its structure; and ii) adjustment of the metal:ligand molar ration, being 1:2.5 for the Fe^{2+}-doped ZIF-9 samples. Therefore the amounts of metal sources and organic ligand are: **ZIF-9_Fe1** ($m_{benzimidazole}$ = 0.210 g, $m_{Co(NO3)2·6H2O}$ = 0.186 g and $m_{FeCl2·4H2O}$ = 0.014 g); **ZIF-9_Fe2** ($m_{benzimidazole}$ = 0.210 g, $m_{Co(NO3)2·6H2O}$ = 0.165 g and $m_{FeCl2·4H2O}$ = 0.028 g); **ZIF-9_Fe3** ($m_{benzimidazole}$ = 0.210 g, $m_{Co(NO3)2·6H2O}$ = 0.145 g and $m_{FeCl2·4H2O}$ = 0.042 g); and **ZIF-9_Fe4** ($m_{benzimidazole}$ = 0.210 g, $m_{Co(NO3)2·6H2O}$ = 0.124 g and $m_{FeCl2·4H2O}$ = 0.057 g).

Pyrolysis of ZIF-9 and Fe^{2+}-doped ZIF-9 compounds

ZIF-9 (0.100 g) was transferred to a quartz tube and placed in a vertical tubular furnace at several temperatures (500, 600, 700, 800 and 900 ºC; heating rate of 5 ºC min^{-1}) for 4 h under a constant N_2 flow of 100 mL·min^{-1}. After 4 h at selected temperature, the resulting pyrolyzed samples (**ZIF-9_Pyrol500**, **ZIF-9_Pyrol600**, **ZIF-9_Pyrol700**, **ZIF-9_Pyrol800** and **ZIF-9_Pyrol900**) were cooled naturally to room temperature. The pyrolysis procedure for Fe^{2+}-doped ZIF-9 samples was the same as described for ZIF-9, except that the pyrolysis was performed at 700 ºC in all the cases.

Electrochemical Measurements

For electrochemical measurements, 4 mg of catalyst was mixed with the same mass of Vulcan carbon and dispersed in 500 µl of N-Methyl-2-pyrrolidone (NMP) using an ultrasonic bath (30 min) to obtain a homogenous ink. A glassy carbon electrode (GCE, ALS Co., Japan) was covered with a catalyst drop-cast of 2 µl (catalyst mass loading of ~0.225 mg·cm^{-2}) and dried at 70 °C for ~30 min. All three-electrode electrochemical measurements were conducted utilizing a *Bio-Logic* (VMP3) multichannel station in a vial sealed with Teflon® cap using modified GCE as the working electrode, Pt spring as counter and Saturated Calomel Electrode

(SCE, Saturated KCl, ALS, RE-2BP) as reference electrode. 0.1 M KOH solution was employed as the electrolyte, saturated with pure oxygen or argon (as the control experiments) using bubbling the gas at into the electrolyte for at least 30 min prior to the experiments. Purging was continued above the solution during the measurements to ensure gas saturation. Cyclic voltammograms (CVs) were collected at a scan rate of 20 mV·s^{-1} after 5 cycles in a potential range of 0.2 to -0.8 V vs. SCE. All electrochemical potentials were reported after a conversion based on the reversible hydrogen electrode (RHE) according to the following equation which stands in 0.1 M KOH:

$$E_{RHE} = E_{SCE} + 0.99 \text{ V} \quad \text{in 0.1 M KOH} \tag{1}$$

PtRuC 20% (FuelCellStore, USA) was examined as commercial catalyst for comparison.

Rotating Disk Electrode (RDE) measurements were conducted by cathodically scanning the modified GCE at a scan rate of 20 mV·s^{-1} with various rotating rates ranging from 400 to 2300 rpm using an RRDE-3A (ALS Co., Ltd) apparatus. Koutecky-Levich theory was employed to mechanistically probe and interpret ORR kinetics. Accordingly, number of transferred electrons (n) was estimated on the basis of following equation:[24]

$$\frac{1}{J} = \frac{1}{J_L} + \frac{1}{J_K} = \frac{1}{B\omega^{1/2}} + \frac{1}{J_K} \tag{2}$$

where J is the experimental current density (mA·cm^{-2}), J_K is kinetic-limiting current density ($J_K = nFkC_{O_2}$), J_L is the diffusion-limiting current density, ω is the angular velocity, and B can be defined as follows:

$$B = 0.62nFC_{O_2}(D_{O_2})^{2/3}v^{-1/6} \tag{3}$$

where F is the Faraday constant (96,485 C·mol^{-1}), C_{O_2} is the bulk concentration of O_2 (1.15×10^{-6} mol·cm^{-3} in 0.1 M KOH), D_{O_2} is the diffusion coefficient of O_2 (1.90×10^{-5} cm^2·s^{-1}), and v is the

kinematic viscosity of the electrolyte (0.01 cm^2·s^{-1}). The kinetic current was estimated from the mass-transport correction of RDE using the following equation:[1]

$$J_K = \frac{(J \times J_L)}{(J_L - J)} \tag{4}$$

The catalytic durability of the samples was examined using chronoamperometric measurements at 0.65 V (ORR) or 1.70 V (OER) vs. RHE at a rotation rate of 1500 rpm in O$_2$ and Ar-saturated 0.1 M KOH solution, respectively.

For Zn-Air battery tests, air cathodes were fabricated by drop-casting of the catalyst ink on gas diffusion layers (FuelCellStore, AvCarb P75T, USA). The catalyst ink was prepared by adding 15 mg of the catalyst and 15 mg of Vulcan carbon to 1.5 ml of absolute ethanol and 50 µl of Nafion solution (5 wt. %). The prepared air cathodes were mounted in a 3D-printed cell with perforations on the cathode side, together with a Zn foil (Goodfellow, UK; purity: 99.9%, 50 µm in thickness) as the anode. The cells were filled with 6 M KOH and 0.02 M ZnSO4 (~3 ml) solution as the electrolyte.

RESULTS AND DISCUSSION

Synthesis of ZIF-9 and Fe²⁺-doped ZIF-9 compounds

ZIF-9 was synthesized according to a previously reported procedure with some modifications (see Experimental Section for further details).[23] Tuning of the metal:ligand molar ratio (1:1 and 1:1.5 for the previously reported and our work, respectively) was needed to isolate the desired phase-pure ZIF-9 (Figure 1a). Despite that, all the other reaction conditions were the same.

Similarly, Fe²⁺-doped ZIF-9 compounds (**ZIF-9_Fe1**, **ZIF-9_Fe2**, **ZIF-9_Fe3** and **ZIF-9_Fe4**), containing different Fe²⁺ content, were prepared by using the same synthetic approach, except changing the metal:ligand molar ratio for 1:2.5 (see Experimental Section). Noteworthy, all Fe²⁺-doped ZIF-9 samples are isostructural to the original ZIF-9 (Figure 1a) and have the same morphology (*i.e.*, block-like particles) with crystalline particles reaching sizes up to *ca.* 200 μm (Figure 1b). Moreover, other complementary solid-state characterization techniques (elemental analysis, FT-IR and N_2 sorption) were employed to prove the purity of all samples and to have insights of their porous nature (see Table S1 and S2, and Figures S1 and S2 in the ESI).

Pyrolysis of ZIF-9 and Fe²⁺-doped ZIF-9 compounds

Aiming the preparation of more efficient Co²⁺- and $(Co_{1-x}Fe_x)^{2+}$-based N-doped carbonaceous bifunctional electrocatalysts, ZIF-9 was pyrolyzed at different temperatures (500, 600, 700, 800 and 900 ºC; obtained materials named as **ZIF-9_Pyrol500**, **ZIF-9_Pyrol600**, **ZIF-9_Pyrol700**, **ZIF-9_Pyrol800** and **ZIF-9_Pyrol900**) and Fe²⁺-doped ZIF-9 compounds at 700 ºC (obtained materials named **ZIF-9_Fe1_Pyrol**, **ZIF-9_Fe2_Pyrol**, **ZIF-9_Fe3_Pyrol** and **ZIF-9_Fe4_Pyrol**) for 4h. PXRD studies reveal that, as expected, all the pyrolyzed compounds are amorphous (Figures S3 in the ESI) and, additionally, characteristic vibrational modes,

corresponding to the organic ligand's functionalities, cannot be identified in the FT-IR spectra (Figures S4 in the ESI). Furthermore, although pyrolyzed ZIF-9 and Fe^{2+}-doped samples have similar morphology to that of the as-prepared ZIF-9, several cracks and defects on their surfaces can be noticed (Figure S5 and S6 in the ESI). This probably originates from the thermal treatment, in which releasing some organic volatiles cause these superficial fissures and defects.

In addition, N_2 sorption measurements showed that Co^{2+}-based N-doped carbonaceous samples possess higher capacity to adsorb N_2, with S_{BET} ranging from 204 to 469 m^2g^{-1}, than the as-prepared ZIF-9 with only 24 m^2g^{-1} (see Figure S7 and Table S3 in the ESI). The employed pyrolysis temperature is the key parameter which dictates the final porosity of the obtained product: samples prepared at lower temperatures have higher BET surface area than those pyrolyzed at higher temperatures. Although less porous than Co^{2+}-based N-doped carbonaceous samples, $(Co_{1-x}Fe_x)^{2+}$-based ones still exhibit higher capacity to adsorb N_2 than the original ZIF-9 (see Figure S8 and Table S3 in the ESI).

Electrocatalysis

The electrocatalytic activity towards the oxygen reduction reaction (ORR) of nanoporous carbons derived from zeolite imidazolate framework (ZIF), more specifically those obtained by pyrolysis of Co-ZIF-9 at various temperatures, was examined through cyclic voltammetry (CV) measurements. The synthesized catalysts were loaded on GCE (as described in the experimental section) and tested in O_2-saturated 0.1 M KOH solution. For the sake of comparison, modified GCE with the same mass loadings were prepared with the commercial PtRuC catalyst (20% Pt/C). Figure S9 depicts CV curves of all pyrolyzed samples and the commercial catalyst in a potential range from 1.2 to 0.2 V vs. RHE using a scan rate of 20 $mV·s^{-1}$. Control experiments were also conducted in Ar-saturated solutions, shown in dashed lines. Almost rectangular CV curves with

no clear cathodic redox peak can be seen for all the samples in the absence of O_2. Conversely, the emergence of an intense clear cathodic peak for all samples in the presence of O_2 reveals catalytic activity of samples toward ORR. Oxygen reduction peak parameters of different samples extracted from Figure S9 are summarized in Table 1. As can be seen, **ZIF-9_Pyrol500** resulted in a poor ORR catalytic activity with an oxygen reduction peak potential (E_p) of 0.72 V and a cathodic peak current (i_p^c) of 0.42 mA·cm^{-2}. This is far behind the catalytic activity of the commercial PtRuC catalyst with a peak potential of 0.79 V and peak current density of 0.50 mA·cm^{-2}. Remarkably, it can be realized from the CV curves that the catalytic activity of the nanoporous carbons improved by increasing the pyrolysis temperature. Accordingly, and as it is evidenced in Table 1, the onset potential (E_{onset}) improved up to 0.89 V in the sample pyrolyzed at 700 °C with a remarkable peak current density of 1.60 mA·cm^{-2} (~ more than three times higher than the commercial catalyst). This may be attributed to the unique composition of the **ZIF-9_Pyrol700** sample arisen from optimized pyrolysis temperature in which high surface area of the sample provides numerous catalytic active sites for ORR. On the other hand, increasing the pyrolysis temperature may result in rearrangement of atoms to form M-N-C bonds which are remarkably favorable sites for O_2 adsorption. The enhancing impact of nitrogen doping on catalytic activity has been extensively studied and attributed to the increased conductivity and atomic charge density in nitrogen doped materials.[25] Enhanced charge density in the course of nitrogen doping will cause spin density asymmetry which facilitates the charge transfer from the carbon network to the adsorbing O_2 molecule. This triggers superoxide formation and weakening O—O bonds, ultimately resulting in enhanced ORR activity by smoothing the path for O—O cleavage.[26-29]

The enhanced electrocatalytic activity of **ZIF-9_Pyrol700** sample compared to the other porous carbons derived at different pyrolysis temperatures might be due to faster reaction kinetics

with a larger net number of electrons per O_2 molecule being transferred during ORR. In order to shed light on the ORR mechanism and kinetics in various samples, linear sweep voltammetry (LSV) measurements were conducted on rotating-disk electrode (RDE) in O_2-saturated 0.1 M KOH solutions. LSV curves of ZIF-9 derived carbons pyrolyzed at various temperatures, recorded at an electrode rotation rate of 1500 rpm with a scan rate of 20 mV·s^{-1} are depicted in Figure 2a. As it is realized from the Figure, LSVs of all samples showed an almost single-step plateau. However, the plateau in **ZIF-9_Pyrol700** is flatter with smaller mixed kinetics-diffusion control region. This suggests higher catalytic activity of **ZIF-9_Pyrol700** in comparison with the other catalysts. Figure 2b shows the extracted parameters (*e.g.*, half-wave potential, $E_{1/2}$; kinetic current density, J_k; and *Tafel* slope) for ORR reaction of different samples. It can be seen that the $E_{1/2}$ grows gradually by increasing the pyrolysis temperature from 0.70 V in **ZIF-9_Pyrol500** with a maximum value of 0.81 V for **ZIF-9_Pyrol700** sample. In addition, the same trend was observed for kinetic current density (J_k) reaching a maximum value of ~2.1 mA·cm^{-2} (almost 40% greater than the one for **ZIF-9_Pyrol500**), suggesting that there are more active sites for ORR in **ZIF-9_Pyrol700** (Figure 2b). The higher kinetic current density in **ZIF-9_Pyrol700** sample suggests larger net number of transferred electrons during ORR which may be attributed to higher number of active M-N-C sites. Overall, these findings are in good agreement with already observed CV results, confirming the superior performance of **ZIF-9_Pyrol700** as an efficient ORR catalyst. This superior ORR electrocatalytic activity performance can be further gleaned from much a smaller *Tafel* slope of 60.4 mV·dec^{-1} at low over-potentials compared to other samples, as shown in Figure 2b. Accordingly, the reaction can attain higher currents at lower over-potentials when using **ZIF-9_Pyrol700** as the catalyst, further implying the superior catalytic performance of this nanoporous carbon among various samples examined in this study.

To further shed light on ORR mechanism, *Koutecky-Levich* theory was utilized to estimate the number of transferred electrons, *n*, during oxygen reduction catalyzed with different samples. Figure 2c shows typical polarization curves for the **ZIF-9_Pyrol700** sample collected at various rotation rates, revealing a well-defined increase in cathodic current density in the mixed kinetics-diffusion control region followed by a plateau in the diffusion-limited area. In Figure 2d *Koutecky-Levich* curves for the samples pyrolyzed at various temperatures can be seen. The linear relationship of reciprocal current with reciprocal square root of the angular velocity implies first-order reaction kinetics with respect to the concentration of dissolved oxygen. Accordingly, the number of transferred electrons (*n*) was estimated from the slope of *Koutecky-Levich* plots for the samples pyrolyzed at various temperatures, shown as the inset of the Figure 2d. It can be seen that the number of electrons increased by increasing the pyrolysis temperature, reaching a maximum value of 3.5 in **ZIF-9_Pyrol700** and **ZIF-9_Pyrol800**. Further increase in pyrolysis temperature diminishes the number of transferred electrons in deterioration in **ZIF-9_Pyrol900**. Together with previous evidences related to onset potential and peak currents, this clearly demonstrates superior ORR performance of **ZIF-9_Pyrol700** in comparison with the others, suggesting that the reaction likely follows a mixed mechanistic fashion operating with 2 and 4 electrons while 4*e* pathway is dominant in **ZIF-9_Pyrol700**. Accordingly, 700 ºC was picked as the optimized pyrolysis temperature and further attempts in this study were focused to surpass the electrocatalytic performance of **ZIF-9_Pyrol700** (*e.g.*, in terms of number of transferred electrons).

In order to enhance the population and efficiency of catalytic active sites, bimetallic ZIF-derived porous carbons were fabricated by synthesis of Fe^{2+}-doped ZIF-9 compounds followed by a pyrolysis step at 700 ºC according to the abovementioned results. Figure 3 shows LSV curves of the samples doped with various amounts of Fe content, respectively named as **ZIF-9_Fe1_Pyrol**

to **ZIF-9_Fe4_Pyrol** according to the amount of Fe content, recorded at an electrode rotation rate of 1500 rpm with a scan rate of 20 mV·s^{-1}. LSVs of all samples showed an almost single-step plateau. It can be seen that inclusion of small amounts of Fe content in samples **ZIF-9_Fe1_Pyrol** and **ZIF-9_Fe2_Pyrol** resulted in slightly deteriorated onset potential and current profile. However, **ZIF-9_Fe3_Pyrol** with increased Fe content showed sharper mixed kinetics-diffusion control region and enhanced limiting current in comparison with its analogue without Fe (*i.e.*, **ZIF-9_Pyrol700**). In order to go deeper in the effect of Fe inclusion on catalytic performance of the samples, extracted parameters from LSV curves are represented in Figure 3b. Interestingly, all of the samples doped with Fe exhibited higher kinetics current density than **ZIF-9_Pyrol700**, demonstrating enhanced catalytic activity of the samples upon doping which can be attributed to the enhanced population of active sites in the bimetallic doped carbons. As it can be readily seen, **ZIF-9_Fe3_Pyrol** exhibited the best catalytic performance among all of the Fe-doped samples. Furthermore, *Koutecky-Levich* theory was employed to estimate the number of transferred electrons. Figure 3c shows typical polarization curves for **ZIF-9_Fe3_Pyrol** collected at various rotation rates. In Figure 3d *Koutecky-Levich* curves for the samples with various Fe content were shown, revealing linear relationship which implies first-order reaction kinetics. Accordingly, the number of transferred electrons (*n*) for various samples were estimated, revealing an increase by increasing the Fe content with a maximum of 3.89 in **ZIF-9_Fe3_Pyrol** (see inset). This observation is in well agreement with the increased kinetic current densities in the case of samples with Fe. Further increase in Fe content in **ZIF-9_Fe4_Pyrol** resulted in decreased number of transferred electrons. Therefore, **ZIF-9_Fe3_Pyrol** sample was chosen as the optimized sample for ORR.

As already stated apart from the ORR, the backward reaction or oxygen evolution reaction (OER) is of great importance, happening during the charge in metal-air batteries. To measure the electrocatalytic activity of samples towards OER, LSV measurements were conducted by anodic scan of the potential from 1.3 to 1.8 V (vs. RHE) in Ar-saturated 0.1 M KOH solutions with a scan rate of 20 mV·s^{-1}. Figure 3e depicts LSV curves for **ZIF-9_Pyrol700** and the samples doped with various amounts of Fe. As can be seen, the sample without Fe (*i.e.*, **ZIF-9_Pyrol700**) exhibited an OER onset of around 1.64 V. Doping of the sample by small amount of Fe (*i.e.* in **ZIF-9_Fe1_Pyrol**) does not significantly change the OER response. However, increasing the Fe-content, the onset potential shifts to lower potentials, resulting in an onset of 1.55 V in the case of **ZIF-9_Fe3_Pyrol** sample. Also the smallest Tafel slope among other catalysts was obtained for **ZIF-9_Fe3_Pyrol**. This clearly demonstrates improved OER catalytic activity of the sample by inclusion of Fe^{2+} in the structure. Additionally, as it is summarized in Figure 3f, **ZIF-9_Fe3_Pyrol** exhibited a drastic decrease in overpotential needed to achieve a current density of 10 mA·cm^{-2} in comparison with the other samples. This excellent OER activity of **ZIF-9_Fe3_Pyrol** is likely attributed to the homogenous distribution of co-doped metallic sites in the porous carbon matrix, providing numerous active sites for the reaction (as it is realized from TEM measurements; Figure 4a-d). Moreover, the presence of Fe likely avoids the agglomeration of Co metallic cores during the pyrolysis. XPS spectrum of **ZIF-9_Fe3_Pyrol** (Figure 4e) exhibits a set of peaks corresponding to C 1s (286.01 eV), N 1s (401.01 eV), O 1s (533.01), Fe 2p (712.01 eV) and Co 2p (780.01 eV). After a peak deconvolution of N 1s (Figures 4f) it was noticed that the aforementioned M-N-C electrocatalytic sites are of three types (*i.e.*, pyridinic-N, pyrrolic-N and graphitic-N). Furthermore, only the pyridinic-N and pyrrolic-N components could be coordinated to both Co^{2+} and Fe^{2+} metallic centers. Remaining deconvoluted spectra, belonging to C 1s, Fe 2p

and Co 2p are represented in Figures S10-13 and the corresponding peak assignment in Tables S4-8. In addition, this excellent OER catalytic activity of **ZIF-9_Fe3_Pyrol** could be further gleaned from a much smaller Tafel slope of 99 mV·dec^{-1}, in comparison with the commercial PtRuC (237 mV·dec^{-1}) catalyst.

The excellent bifunctional catalytic activity of **ZIF-9_Fe3_Pyrol** can be also realized from its small ΔE value ($\Delta E = E_{j=10} - E_{1/2}$, as a well-known bifunctional performance descriptor for oxygen electrodes). As it can be seen in Figure 5a, this value comes out at 0.81 V for **ZIF-9_Fe3_Pyrol** which is nearly as small as the state-of-the-art commercial PtRuC sample ($\Delta E = 0.8$ V). Additionally, it can be seen that in the ORR branch the mixed kinetics-diffusion control region for **ZIF-9_Fe3_Pyrol** is much smaller than the PtRuC catalyst. The same observation can be also learned in OER branch where both samples reach a current density of 10 mA·cm^{-2} in the same overpotential. This is in well agreement with much smaller Tafel slope obtained for **ZIF-9_Fe3_Pyrol**, revealing its excellent activity towards oxygen reactions. Figure 5b depicts the comparison of ΔE values for all the measured catalysts in this study, showing that **ZIF-9_Fe3_Pyrol** possesses the smallest value among other synthesized samples. Table 2 compares the electrocatalytic behavior of the **ZIF-9_Fe3_Pyrol** sample with some recently reported MOF-derived bifunctional electrocatalysts for ORR/OER. As can be seen from the table, **ZIF-9_Fe3_Pyrol** sample exhibited superior or comparable catalytic activity, suggesting **ZIF-9_Fe3_Pyrol** sample as a promising and efficient bifunctional electrocatalyst towards ORR/OER reactions.

Electrocatalytic activity stability of **ZIF-9_Fe3_Pyrol** towards ORR and OER was also examined and compared with commercial PtRuC catalyst through chronoamperometric measurements in 0.1 M KOH solution at a rotation rate of 1500 rpm. As seen in Figure 5c, **ZIF-**

9_Fe3_Pyrol could excellently retain around 82 and 78% of its initial cathodic and anodic currents in ORR and OER, respectively. This is while that in both reactions PtRuC exhibited inferior activity durability. This clearly displays that, while commercial PtRuC catalyst only provided low long-term ORR/OER currents, **ZIF-9_Fe3_Pyrol** could remain stable much longer under the same conditions, demonstrating superior long-term performance as a bifunctional catalyst. All of the obtained results support the promising catalytic characteristics of **ZIF-9_Fe3_Pyrol** as an efficient non-precious bifunctional electrocatalyst for reversible oxygen reduction or evolution reactions with excellent durability.

According to the obtained results, we further examined the practical application of **ZIF-9_Fe3_Pyrol** as the air cathode in rechargeable Zn-air batteries (Figure 6). Figure 6a shows the discharge profiles at 5 mA·cm^{-2} for the Zn-air batteries, revealing a stable voltage plateau of ~1.25 V and a high specific capacity of 815 mAh·g^{-1} (corresponding to a high energy density of 1018·Wh·kg$_{Zn}^{-1}$), significantly higher than the battery with state-of-the-art catalyst. Figure 5b displays the galvanodynamic discharge profiles as well as their corresponding power density curves for the cells assembled with **ZIF-9_Fe3_Pyrol** and PtRuC samples as cathode catalysts. As it can be seen, in the case of the battery including **ZIF-9_Fe3_Pyrol**, a peak power density of 32 mW·cm^{-2} achieved at 57 mA·cm^{-2}, comparable with the battery assembles with PtRuC commercial catalyst. Discharge profiles of the Zn-air batteries with **ZIF-9_Fe3_Pyrol** and PtRuC samples as the oxygen electrode at various specific currents are shown in Figure 6c. The battery with **ZIF-9_Fe3_Pyrol** provided almost stable plateaus in all different current loads (*e.g.*, 1.15 V at 20 mA·cm^{-2}), outperforming the assembled device with PtRuC, especially at high rates. The charge-discharge profiles of Zn-air batteries with **ZIF-9_Fe3_Pyrol** and PtRu/C oxygen catalyst electrodes are shown in Figure 6d and e. A small round-trip voltage difference of only 0.75 V was

seen for the device loaded with the bimetallic ZIF-derived N-doped porous carbon which is around 50 mV lower than the one obtained with PtRuC air cathode (round-trip voltage difference of 0.80 V). This clearly verifies the superior bifunctional catalytic activity of **ZIF-9_Fe3_Pyrol**. More importantly, it can be seen that the round-trip voltage difference of **ZIF-9_Fe3_Pyrol** gradually increased reaching a value of 1.02 V after 15h (36% increase in round-trip voltage difference). This is by far smaller than increased charge/discharge voltage difference (~2.34 V) for PtRu/C electrode (192% increase in round-trip voltage difference). This further demonstrates high ORR/OER bifunctional activity and excellent catalytic durability of **ZIF-9_Fe3_Pyrol** as an air cathode for rechargeable Zn-air batteries. All of these results suggest **ZIF-9_Fe3_Pyrol** as an excellent bifunctional catalyst for rechargeable Zn-air batteries batteries.

CONCLUSION

In summary, we synthesized bimetal Co-, Fe-, and N- co-doped carbons through Fe^{2+} doping of ZIF-9 metal organic frameworks followed by a pyrolysis step and investigated their electrocatalytic activity for oxygen reduction (ORR) and evolution (OER) reactions. The synthetic conditions (*e.g.*, the pyrolysis temperature and Fe content) were optimized with an aim of improving electrochemical performance. According to the obtained results, **ZIF-9_Fe3_Pyrol** outperformed the other samples, in terms of more positive onset potentials and cathodic current densities for ORR. Rotating disk (RDE) measurements verified that **ZIF-9_Fe3_Pyrol** catalyzes ORR mainly from a 4*e* process, the same mechanism in commercial Pt-based catalysts. In addition, the **ZIF-9_Fe3_Pyrol** catalyst outperformed the commercial catalyst in terms of electrocatalytic durability. Evaluation of the electrocatalytic activity of **ZIF-9_Fe3_Pyrol** for OER demonstrated excellent behavior and durability. Finally, **ZIF-9_Fe3_Pyrol** exhibited excellent performance as an air cathode when assembled in a rechargeable Zn-air battery, resulting in a high capacity of 815 $mAh \cdot g^{-1}$ and energy density of 1018 $Wh \cdot kg_{Zn}^{-1}$. A superior cycling stability as compared to the state-of-the-art PtRuC-loaded air cathode has also been demonstrated, suggesting **ZIF-9_Fe3_Pyrol** sample as a promising bifunctional catalyst for ORR/OER in energy storage applications.

ASSOCIATED CONTENT

Supporting Information

The Supporting Information is available free of charge on the ACS Publications website at DOI:

Several Figures and Tables concerning elemental analysis, FT-IR, N_2 sorption, PXRD, SEM, CV

Curves and XPS measurements for the reported samples can be found.

AUTHOR INFORMATION

Corresponding Author

*E-mail: patricia.horcajada@imdea.org; rebeca.marcilla@imdea.org

ORCID

Afshin Pendashteh: 0000-0002-9884-3721

Sérgio M. F. Vilela: 0000-0001-5125-1676

Jesus Palma: 0000-0003-1022-0165

Patricia Horcajada: 0000-0002-6544-5911

Rebeca Marcilla: 0000-0002-5660-6381

Notes

The authors declare no competing financial interest.

ACKNOWLEDGEMENRS

TABLE 1

Table 1. Electrochemical parameters extracted from CV curves in Figure 2.

Sample	E_{onset} (V vs. RHE)	E_p (V vs. RHE)	i_p^c (mA.cm^{-2})
PtRuC	0.92	0.79	0.50
ZIF-9_Pyrol500	0.81	0.72	0.42
ZIF-9_Pyrol600	0.88	0.79	0.77
ZIF-9_Pyrol700	0.89	0.76	1.60
ZIF-9_Pyrol800	0.87	0.77	0.66
ZIF-9_Pyrol900	0.85	0.79	0.55

TABLE 2

Table 2. Comparison of electrocatalytic activity of the ZIF-9_Fe3_Pyrol sample with some recently reported MOF-derived bifunctional catalysts.

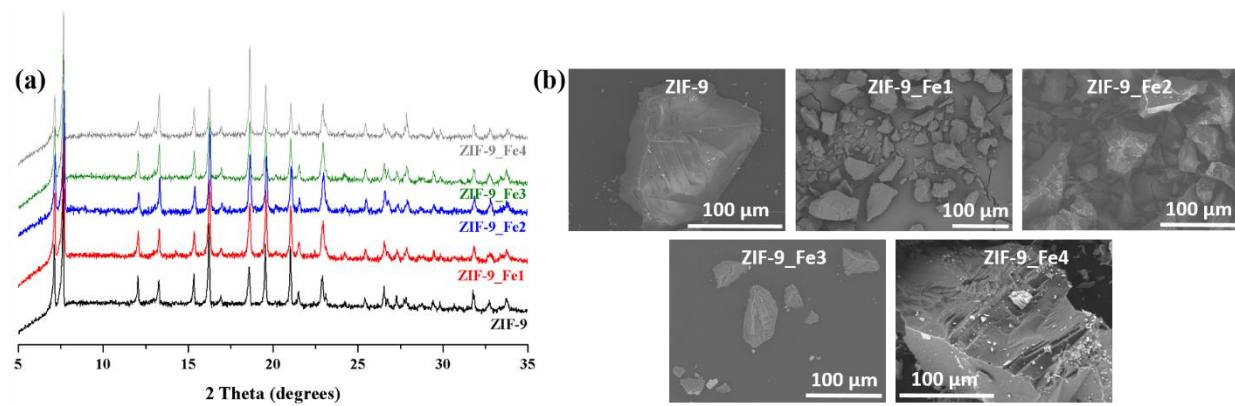| Sample	E_{onset}^{ORR} (V vs. RHE)	n_e	Tafel Slope ORR (mV.dec^{-1})	E_{onset}^{OER} (V vs. RHE)	Tafel Slope OER (mV.dec^{-1})	ΔE(V)	Reference
ZIF-9_Fe3_Pyrol	0.90	3.89	55	1.55	99	0.81	This Work
BNPC-1000	0.89	3.70	80	1.38	201	-	[30]
Co@C-800	0.92	~4	-	1.43	106	-	[31]
ZnCoNC-0.1	0.90	-	66	-	130	-	[32]
HC-5Co95Zn	0.96	~3.90	-	-	-	0.82	[33]
The Co-MOF@CNTs	0.91	3.70	-	1.51	69	-	[34]

FIGURE 1

Figure 1. (a) PXRD patterns and **(b)** SEM images of the original ZIF-9 and the isotypical Fe^{2+}-doped ZIF-9 compounds.
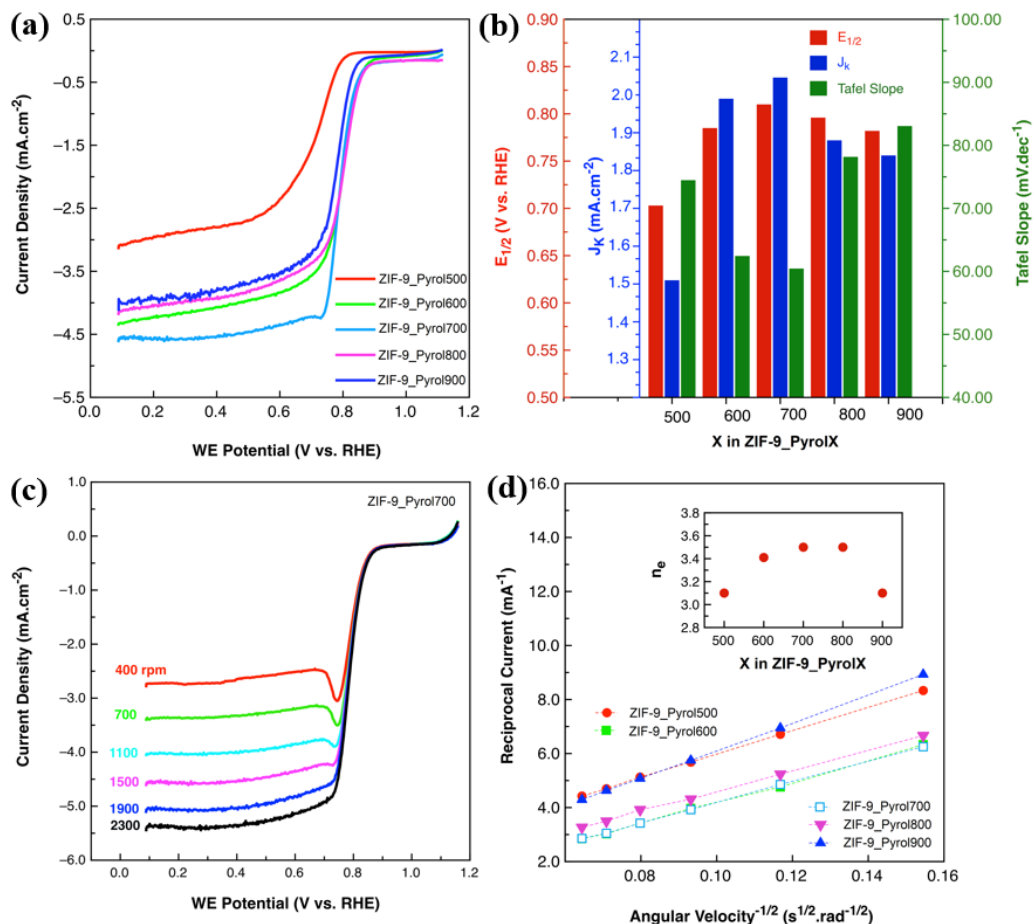
FIGURE 2

Figure 2. (a) Rotating disk LSV profiles of the prepared samples pyrolyzed at various temperatures in O_2-saturated 0.1 M KOH solution at a rotation rate of 1500 rpm with a scan rate of 20 mV s^{-1}. **(b)** Extracted parameters including half-wave potential ($E_{1/2}$), kinetic current density (J_k), and *Tafel* slopes for porous carbons derived at various pyrolysis temperature. **(c)** RDE-LSV curves for **ZIF-9_Pyrol700** sample at various rotation rates. **(d)** *Koutecky-Levich* plot for the **ZIF-9_Pyrol700** sample and the estimated number of transferred electrons for various samples prepared at different pyrolysis temperature (inset).
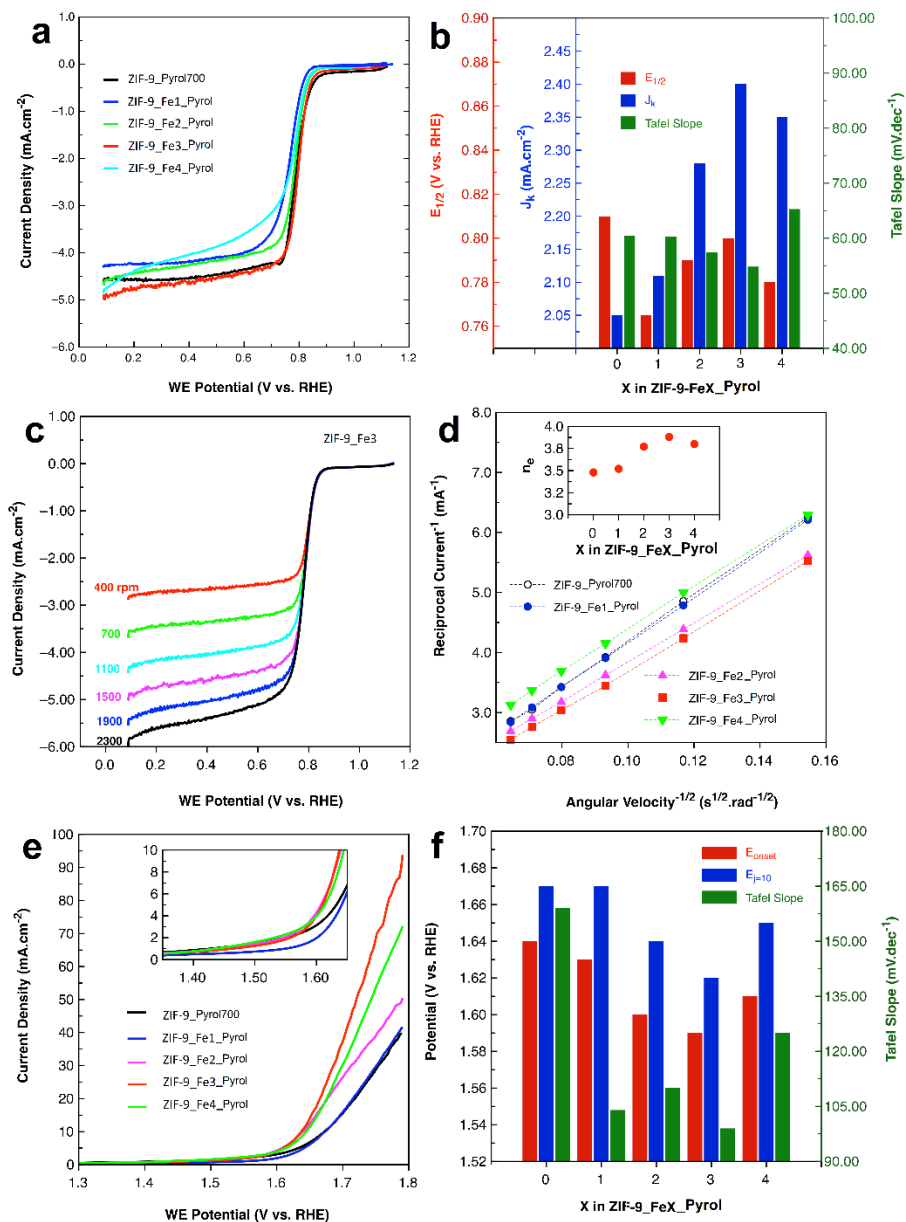
FIGURE 3

Figure 3. **(a)** Rotating disk LSV profiles of the prepared samples with various Fe^{2+} content in O_2-saturated 0.1 M KOH solution at a rotation rate of 1500 rpm with a scan rate of 20 mV·s^{-1}. **(b)** Extracted parameters including half-wave potential ($E_{1/2}$), kinetic current density (J_k), and *Tafel* slopes for porous carbons with different amount of Fe^{2+}. **(c)** RDE-LSV curves for **ZIF-9_Fe3_Pyrol** sample at various rotation rates. **(d)** *Koutecky-Levich* plots for the samples and their

corresponding number of transferred electrons (inset). **(e)** Rotating disk LSV profiles of the prepared samples with various Fe^{2+} content in the OER region with a scan rate of 20 mV·s^{-1}. **(f)** Extracted parameters including onset potential (E_{onset}), overpotential needed to achieve 10 mA·cm^{-2}, and *Tafel* slopes for porous carbons with different amount of Fe^{2+}.
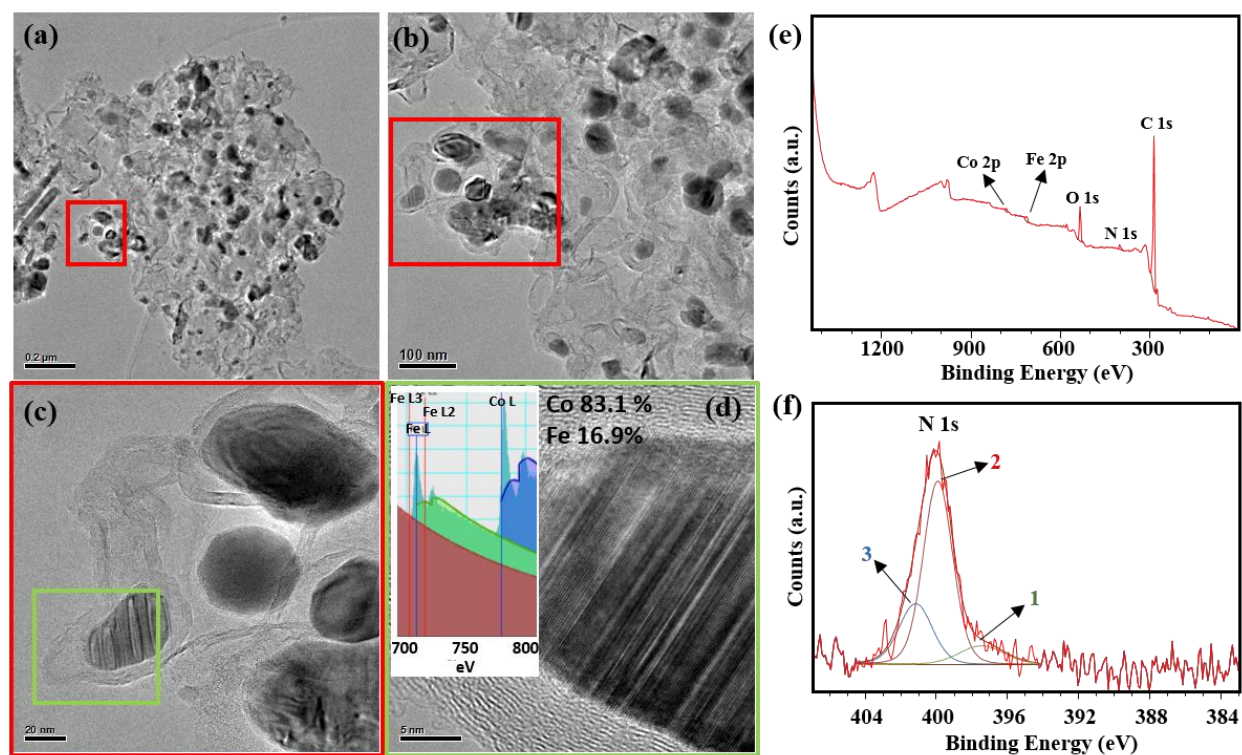
FIGURE 4

Figure 4. (a-c) TEM images at different magnifications of a selected area of **ZIF-9_Fe3_Pyrol**, showing the co-doped metallic sites (dark spots) homogeneously distributed in the N-doped carbon matrix. **(d)** XEDS microanalysis suggests a Co:Fe atomic ration of ~1:5, agreeing well with elemental analysis (Table S1); **(e)** XPS survey of **ZIF-9_Fe3_Pyrol**; and **(f)** Deconvoluted XPS N 1s binding energy spectrum of **ZIF-9_Fe3_Pyrol** with three peaks centered at 397.45 (**1**), 399.91 (**2**) and 401.16 eV (**3**) attributed to pyridinic-N, pyrrolic-N and graphitic-N, respectively.
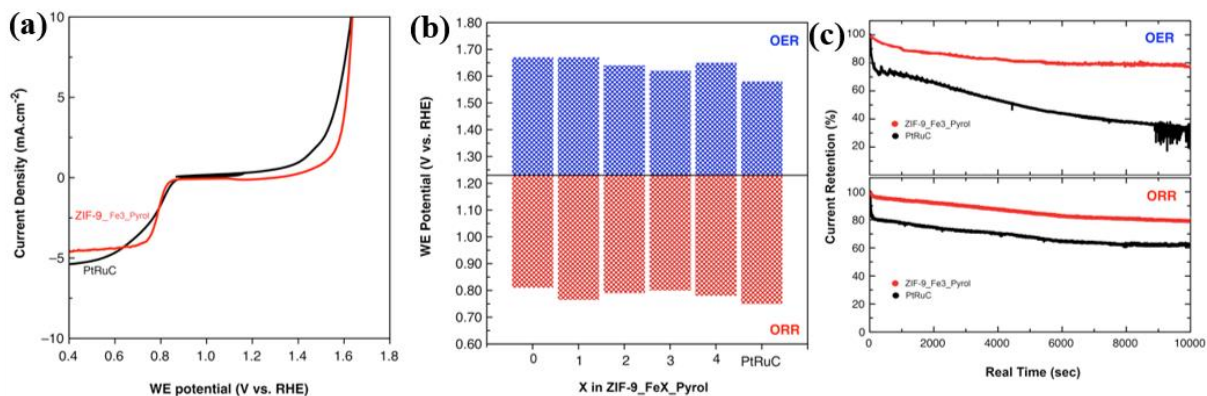
FIGURE 5

Figure 5. (a) Bifunctional electrocatalytic performance of **ZIF-9_Fe3_Pyrol**; **(b)** Comparison of ΔE value ($\Delta E = E_{j=10} - E_{1/2}$) for different samples, and **(c)** ORR and OER catalytic durability of **ZIF-9_Fe3_Pyrol** in comparison with commercial PtRuC catalyst.
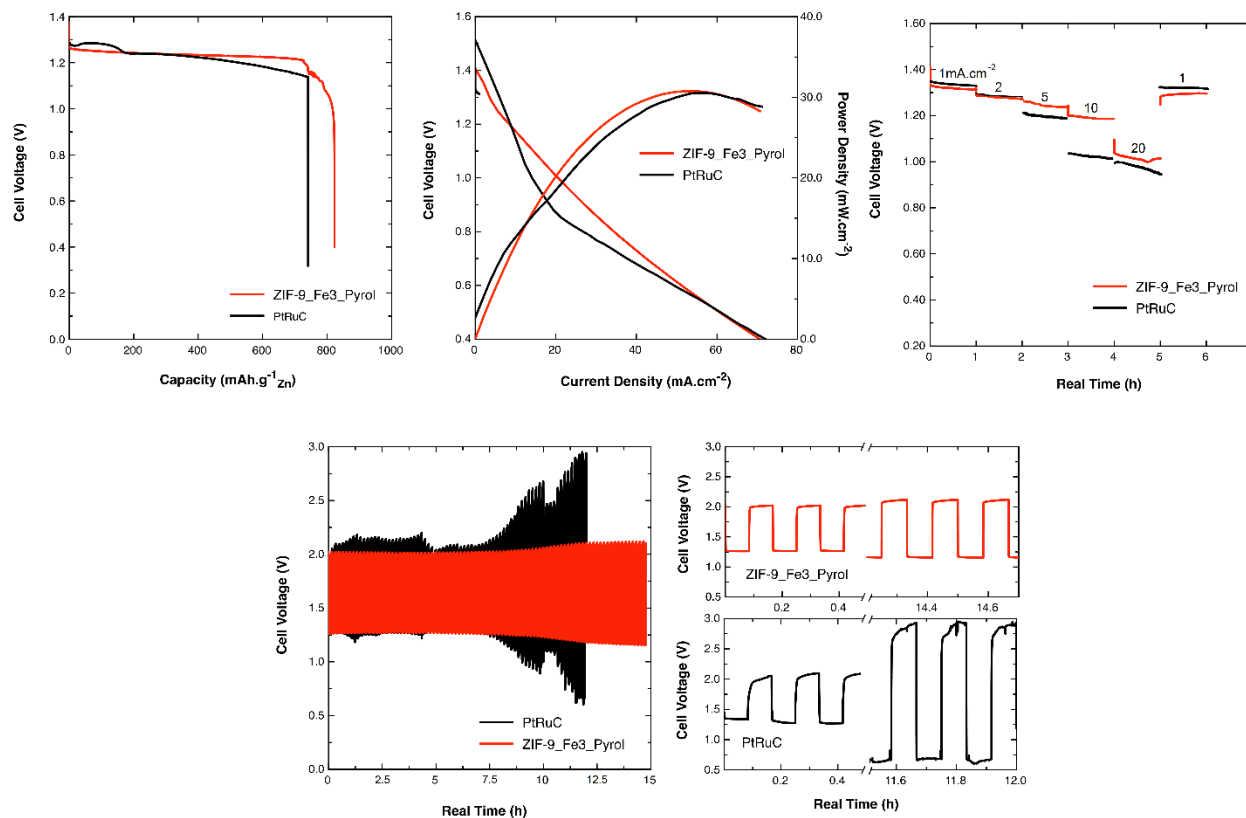
FIGURE 6

Figure 6. (*a*) Discharge profiles of Zn-air batteries with **ZIF-9_Fe3_Pyrol** and PtRuC samples as oxygen electrode catalysts at a discharge current density of 5 mA·cm^{-2}. **(b)** Galvanodynamic discharge profile and power density of the samples. **(c)** Discharge profiles of the Zn-air batteries at various current densities. **(d, e)** Charge-discharge profiles of Zn-air batteries with **ZIF-9_Fe3_Pyrol** and PtRuC samples as oxygen catalysts at 2 mA·cm^{-2}.

REFERENCES

1.   Ge, X.; Sumboja, A.; Wuu, D.; An, T.; Li, B.; Goh, F. W. T.; Hor, T. S. A.; Zong, Y.; Liu, Z., Oxygen Reduction in Alkaline Media: From Mechanisms to Recent Advances of Catalysts. *ACS Catal.* **2015,** *5* (8), 4643-4667.
2.   Stoerzinger, K. A.; Risch, M.; Suntivich, J.; Lu, W. M.; Zhou, J.; Biegalski, M. D.; Christen, H. M.; Ariando; Venkatesan, T.; Shao-Horn, Y., Oxygen electrocatalysis on (001)-oriented manganese perovskite films: Mn valency and charge transfer at the nanoscale. *Energy & Environmental Science* **2013,** *6* (5), 1582-1588.
3.   Liang, Y.; Li, Y.; Wang, H.; Zhou, J.; Wang, J.; Regier, T.; Dai, H., Co3O4 nanocrystals on graphene as a synergistic catalyst for oxygen reduction reaction. *Nat. Mater.* **2011,** *10* (10), 780-786.
4.   Qing, W.; Lu, S.; Run, S.; Xin, Z.; Yufei, Z.; N., W. G. I.; Li-Zhu, W.; Chen-Ho, T.; Tierui, Z., NiFe Layered Double Hydroxide Nanoparticles on Co,N-Codoped Carbon Nanoframes as Efficient Bifunctional Catalysts for Rechargeable Zinc–Air Batteries. *Adv. Energy Mater.* **2017,** *7* (21), 1700467.
5.   Zhiming, C.; Gengtao, F.; Yutao, L.; B., G. J., Ni3FeN-Supported Fe3Pt Intermetallic Nanoalloy as a High-Performance Bifunctional Catalyst for Metal–Air Batteries. *Angew. Chem. Int. Ed.* **2017,** *56* (33), 9901-9905.
6.   Han, X.; Wu, X.; Zhong, C.; Deng, Y.; Zhao, N.; Hu, W., NiCo2S4 nanocrystals anchored on nitrogen-doped carbon nanotubes as a highly efficient bifunctional electrocatalyst for rechargeable zinc-air batteries. *Nano Energy* **2017,** *31*, 541-550.
7.   Pendashteh, A.; Palma, J.; Anderson, M.; Vilatela, J. J.; Marcilla, R., Doping of Self-Standing CNT Fibers: Promising Flexible Air-Cathodes for High-Energy-Density Structural Zn–Air Batteries. *ACS Applied Energy Materials* **2018,** *1* (6), 2434-2439.
8.   Stoerzinger, K. A.; Risch, M.; Han, B.; Shao-Horn, Y., Recent Insights into Manganese Oxides in Catalyzing Oxygen Reduction Kinetics. *ACS Catal.* **2015,** *5* (10), 6021-6031.
9.   Liang, Y.; Wang, H.; Zhou, J.; Li, Y.; Wang, J.; Regier, T.; Dai, H., Covalent Hybrid of Spinel Manganese–Cobalt Oxide and Graphene as Advanced Oxygen Reduction Electrocatalysts. *J. Am. Chem. Soc.* **2012,** *134* (7), 3517-3523.
10.   Dong, C.; Liu, Z.-W.; Liu, J.-Y.; Wang, W.-C.; Cui, L.; Luo, R.-C.; Guo, H.-L.; Zheng, X.-L.; Qiao, S.-Z.; Du, X.-W.; Yang, J., Modest Oxygen-Defective Amorphous Manganese-Based Nanoparticle Mullite with Superior Overall Electrocatalytic Performance for Oxygen Reduction Reaction. *Small* **2017,** *13* (16), 1603903-n/a.
11.   Su, C.-Y.; Cheng, H.; Li, W.; Liu, Z.-Q.; Li, N.; Hou, Z.; Bai, F.-Q.; Zhang, H.-X.; Ma, T.-Y., Atomic Modulation of FeCo–Nitrogen–Carbon Bifunctional Oxygen Electrodes for Rechargeable and Flexible All-Solid-State Zinc–Air Battery. *Adv. Energy Mater.* **2017,** *7* (13), 1602420-n/a.
12.   Kitagawa, S.; Kitaura, R.; Noro, S.-i., Functional Porous Coordination Polymers. *Angew. Chem. Int. Ed.* **2004,** *43* (18), 2334-2375.
13.   Rowsell, J. L. C.; Yaghi, O. M., Metal–organic frameworks: a new class of porous materials. *Microporous and Mesoporous Materials* **2004,** *73* (1), 3-14.
14.   Férey, G., Hybrid porous solids: past, present, future. *Chemical Society Reviews* **2008,** *37* (1), 191-214.
15.   Furukawa, H.; Cordova, K. E.; O'Keeffe, M.; Yaghi, O. M., The Chemistry and Applications of Metal-Organic Frameworks. *Science* **2013,** *341* (6149).

16.   Farha, O. K.; Eryazici, I.; Jeong, N. C.; Hauser, B. G.; Wilmer, C. E.; Sarjeant, A. A.; Snurr, R. Q.; Nguyen, S. T.; Yazaydın, A. Ö.; Hupp, J. T., Metal–Organic Framework Materials with Ultrahigh Surface Areas: Is the Sky the Limit? *J. Am. Chem. Soc.* **2012,** *134* (36), 15016-15021.

17.   Qiu, S.; Xue, M.; Zhu, G., Metal–organic framework membranes: from synthesis to separation application. *Chemical Society Reviews* **2014,** *43* (16), 6116-6140.

18.   Getman, R. B.; Bae, Y.-S.; Wilmer, C. E.; Snurr, R. Q., Review and Analysis of Molecular Simulations of Methane, Hydrogen, and Acetylene Storage in Metal–Organic Frameworks. *Chemical Reviews* **2012,** *112* (2), 703-723.

19.   Liu, H.; Xu, C.; Li, D.; Jiang, H.-L., Photocatalytic Hydrogen Production Coupled with Selective Benzylamine Oxidation over MOF Composites. *Angew. Chem. Int. Ed.* **2018,** *57* (19), 5379-5383.

20.   Chen, Y.; Wang, D.; Deng, X.; Li, Z., Metal–organic frameworks (MOFs) for photocatalytic CO2 reduction. *Catal. Sci. Technol.* **2017,** *7* (21), 4893-4904.

21.   Ramaswamy, P.; Wong, N. E.; Shimizu, G. K. H., MOFs as proton conductors – challenges and opportunities. *Chemical Society Reviews* **2014,** *43* (16), 5913-5932.

22.   Zhao, Y.; Song, Z.; Li, X.; Sun, Q.; Cheng, N.; Lawes, S.; Sun, X., Metal organic frameworks for energy storage and conversion. *Energy Storage Materials* **2016,** *2*, 35-62.

23.   Park, K. S.; Ni, Z.; Côté, A. P.; Choi, J. Y.; Huang, R.; Uribe-Romo, F. J.; Chae, H. K.; O'Keeffe, M.; Yaghi, O. M., Exceptional chemical and thermal stability of zeolitic imidazolate frameworks. *Proceedings of the National Academy of Sciences* **2006,** *103* (27), 10186.

24.   Sun, M.; Dong, Y.; Zhang, G.; Qu, J.; Li, J., [small alpha]-Fe2O3 spherical nanocrystals supported on CNTs as efficient non-noble electrocatalysts for the oxygen reduction reaction. *J. Mater. Chem. A* **2014,** *2* (33), 13635-13640.

25.   Bayram, E.; Yilmaz, G.; Mukerjee, S., A solution-based procedure for synthesis of nitrogen doped graphene as an efficient electrocatalyst for oxygen reduction reactions in acidic and alkaline electrolytes. *Appl. Catal., B* **2016,** *192*, 26-34.

26.   Chen, Z.; Higgins, D.; Tao, H.; Hsu, R. S.; Chen, Z., Highly Active Nitrogen-Doped Carbon Nanotubes for Oxygen Reduction Reaction in Fuel Cell Applications. *J. Phys. Chem. C* **2009,** *113* (49), 21008-21013.

27.   Wu, Z.-S.; Yang, S.; Sun, Y.; Parvez, K.; Feng, X.; Müllen, K., 3D Nitrogen-Doped Graphene Aerogel-Supported Fe3O4 Nanoparticles as Efficient Electrocatalysts for the Oxygen Reduction Reaction. *J. Am. Chem. Soc.* **2012,** *134* (22), 9082-9085.

28.   Guo, D.; Shibuya, R.; Akiba, C.; Saji, S.; Kondo, T.; Nakamura, J., Active sites of nitrogen-doped carbon materials for oxygen reduction reaction clarified using model catalysts. *Science* **2016,** *351* (6271), 361-365.

29.   Pendashteh, A.; Palma, J.; Anderson, M.; Marcilla, R., NiCoMnO4 nanoparticles on N-doped graphene: Highly efficient bifunctional electrocatalyst for oxygen reduction/evolution reactions. *Appl. Catal., B* **2017,** *201*, 241-252.

30.   Qian, Y.; Hu, Z.; Ge, X.; Yang, S.; Peng, Y.; Kang, Z.; Liu, Z.; Lee, J. Y.; Zhao, D., A metal-free ORR/OER bifunctional electrocatalyst derived from metal-organic frameworks for rechargeable Zn-Air batteries. *Carbon* **2017,** *111*, 641-650.

31.   Chen, B.; Ma, G.; Zhu, Y.; Xia, Y., Metal-organic-frameworks derived cobalt embedded in various carbon structures as bifunctional electrocatalysts for oxygen reduction and evolution reactions. *Sci. Rep.* **2017,** *7* (1), 5266.

32.	Wu, X.; Meng, G.; Liu, W.; Li, T.; Yang, Q.; Sun, X.; Liu, J., Metal-organic framework-derived, Zn-doped porous carbon polyhedra with enhanced activity as bifunctional catalysts for rechargeable zinc-air batteries. *Nano Research* **2018,** *11* (1), 163-173.

33.	Meng, Z.; Cai, H.; Tang, H., BimetallicZeolitic Imidazolate Framework-derived Porous Carbon as Efficient Bifunctional Electrocatalysts for Zn-air Battery. *Int. J. Electrochem. Sci* **2018,** *13*, 5788-5797.

34.	Fang, Y.; Li, X.; Li, F.; Lin, X.; Tian, M.; Long, X.; An, X.; Fu, Y.; Jin, J.; Ma, J., Self-assembly of cobalt-centered metal organic framework and multiwalled carbon nanotubes hybrids as a highly active and corrosion-resistant bifunctional oxygen catalyst. *J. Power Sources* **2016,** *326*, 50-59.